Dual-Use Multicarrier Waveform for Radar Detection and Communication

JOHN ELLINGER, Member, IEEE
Wright-Patterson Air Force Base, Dayton, OH, USA

ZHIPING ZHANG, Member, IEEE
ZHIQIANG WU, Senior Member, IEEE
Wright State University, Dayton, OH, USA

MICHAEL C. WICKS, Fellow, IEEE
University of Dayton Research Institute, Dayton, OH, USA

The use of multicarrier waveforms, such as *orthogonal frequency division multiplexing* (OFDM) as used in radio communication, is gaining interest within the radar community. This paper considers the optimization of radar performance within the structure imposed by a coded OFDM format required to achieve an acceptable communication link. The dual goal of achieving both satisfactory radar and communication performance raises challenges that can be substantively addressed by combining phase coding and modulation techniques to provide the temporal and spectral structure necessary to implement simultaneous radar and communication operations.

Manuscript received May 16, 2016; revised November 17, 2016; released for publication April 20, 2017. Date of publication December 6, 2017; date of current version June 7, 2018.

DOI. No. 10.1109/TAES.2017.2780578

Refereeing of this contribution was handled by F. Gini.

Authors' addresses: J. Ellinger is with the United States Department of the Air Force, Wright-Patterson Air Force Base, Dayton, OH 45433 USA, E-mail: (john.ellinger@us.af.mil); Z. Zhang and Z. Wu are with the Department of Electrical Engineering, Wright State University, Dayton, OH 45435 USA, E-mail: (Zhang.176@wright.edu; Zhiqiang.wu@wright.edu); M. C. Wicks is with the University of Dayton Research Institute, Dayton, OH 45469 USA, E-mail: (Michael.Wicks@udri.udayton.edu). *(Corresponding author: Zhiqiang Wu.)*

I. INTRODUCTION

Due in part to the success of multicarrier waveforms, such as *orthogonal frequency division multiplexing* (OFDM) in radio communication technologies, the use of spread spectrum waveforms has gained strong interested within the radar community. From a radar-centric point of view, multicarrier waveforms can be used to improve detection and measurement performance [1]–[3]. Furthermore, the use of such waveforms improves resistance to multipath fading [4], [5], the ability to overcome the limitations of a congested frequency spectrum [6], the ability to exploit frequency diversity gains stemming from the fact that target scattering centers inherently resonate differently at different frequencies [7], and the potential to perform radar and communication functions simultaneously within the same hardware using the same waveform [8]–[10]. In comparison to traditional single carrier systems, a multicarrier radar provides more degrees of freedom in waveform synthesis.

The range (or delay) resolution of a radar system is inversely proportional to the transmitted signal bandwidth. Realizing that improving range resolution usually entails employing a shorter bit duration in a digital phase modulated system or a wider frequency spread in an analog frequency modulated system, Levanon [11]–[13], and Levanon and Mozeson [14], [15] borrowed ideas from wireless digital communications to improve radar measurement performance. In digital communications, there is a similar problem where it is desired to increase the transmission efficiency. This can be accomplished by employing a shorter bit duration and increasing the frequency spread of the communication transmission. Noting that the modulation technique OFDM is one such way of increasing transmission efficiency, Levanon and Mozeson employ OFDM to modulate *Multifrequency complementary phase-coded* (MCPC) sequences to improve radar detection performance. Our research expands on the works of Levanon and Mozeson by employing their use of OFDM to modulate MCPC sequences to allow for both radar and communication operations.

This paper considers the optimization of radar performance within the structure imposed by a coded OFDM format required to achieve an acceptable communication link. The dual goal of achieving both satisfactory radar and communication performance raises challenges that can be substantively addressed by combining phase coding and modulation techniques to provide the temporal and spectral structure necessary to implement simultaneous radar and communication operations.

II. MCPC SIGNALS

The seminal work of Levanon[11]–[13], and Levanon and Mozeson [14], [15] examined the use of multicarrier communication technologies and MCPC sequences to increase the range resolution of radar systems. MCPC signals are sequences of signals, each different from one another, that form a complementary set. A complementary set is defined as cyclically shifted versions of a phase-coded

TABLE I
Phases in Degrees of the Elements of a P3-Based 5× 5 MCPC Signal

0	−144	−216	−216	−144
−144	−216	−216	−144	0
−216	−216	−144	0	−144
−216	−144	0	−144	−216
−144	0	−144	−216	−216

sequence having an ideal periodic *autocorrelation function* (ACF) [16]. Two such codes (which form the basis of MCPC signals) are the polyphase P3 and P4 code sequences. The phase terms of an M length P3 code are constructed as

$$\phi_m = \frac{\pi}{M}(m-1)^2 - \pi(m-1) \tag{1}$$

for $m = 1, 2, \ldots, M$, and the phase terms for an M length P4 code are constructed as

$$\phi_m = \begin{cases} \dfrac{\pi}{M}(m-1)^2 & m \text{ is even} \\ \dfrac{\pi}{M}(m-1)\,m & m \text{ is odd} \end{cases} \tag{2}$$

for $m = 1, 2, \ldots, M$. The MCPC signal is an $M \times M$ matrix of cyclically shifted versions of either M length P3 or M length P4 codes. It is possible to stack MCPC sequences resulting in an $N \times M$ sequence where N is an integer multiple of M. Such a stacked sequence also forms a complementary set. Table I provides an example of a P3-based 5×5 MCPC signal.

Using a traditional OFDM signaling scheme, the M sequences are transmitted on N subcarriers separated in frequency by

$$\Delta f = \mathrm{BW}/N = 1/t_b \tag{3}$$

where BW is the bandwidth of the system, and t_b is the time duration of each bit in the sequence. The total duration of the transmitted pulse is then Mt_b. The transmitted pulse is mathematically defined as

$$X(t) = \sum_{n=1}^{N} \exp\left(j2\pi t \Delta f \left(\frac{N+1}{2} - n\right)\right) \cdot \sum_{m=1}^{M} u_{n,m}(t - (m-1)t_b) \tag{4}$$

where

$$u_{n,m} = \begin{cases} \exp(j\phi_{n,m}) & 0 \le t \le t_b \\ 0 & \text{otherwise} \end{cases} \tag{5}$$

and $\phi_{n,m}$ is the mth phase element of the nth sequence (i.e., the mth column and nth row of Table I). It is observed that this OFDM modulation scheme can be efficiently accomplished with the *inverse fast Fourier transform* (FFT) operation and that, upon reception, the transmitted sequence can be demodulated through the application of the FFT.

A measure of performance of a radar signal is its autocorrelation sidelobe response. A typical approach to reduce sidelobe levels is to apply a weighting (i.e., a Hamming window) to the transmitted pulse. This weighting results in reduced sidelobes with the consequence of a wider center response, which causes a reduction in range measurement accuracy. Fig. 1 compares the autocorrelation response of an MCPC P3 signal, an linear frequency modulated (LFM) signal that has a total bandwidth to provide the same range measurement resolution as the P3 signal, and the same LFM signal with a Hamming window applied. It is clear that the windowed signal produces much lower sidelobes at the cost of a wider center response and that the sidelobe levels of the P3 signal are much larger than the others.

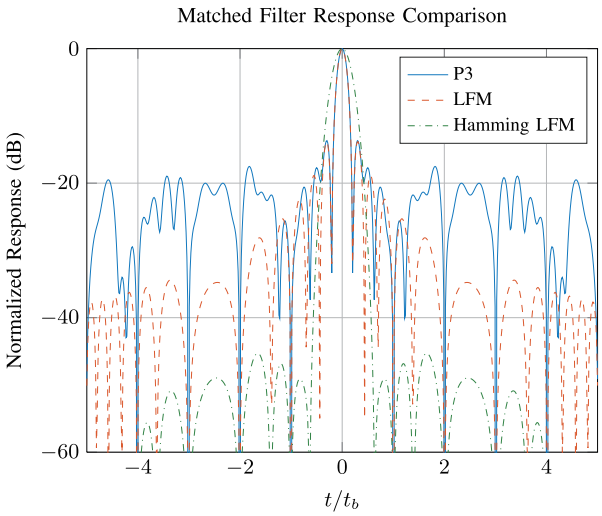

Fig. 1. Normalized ACF of a 5 × 5 P3-based MCPC signal (labeled P3) is compared with an LFM signal (labeled LFM) and a LFM signal with a Hamming weight applied (labeled H-LFM). The P3 signal exhibits ideal periodic sidelobes at integer multiples of t/t_b.

III. POLAR SIGNAL DETECTION (PSD)

It is clear that maximizing the *probability of detection* (P_D) is equivalent to maximizing the SNR at the output of the receive filter. As described in [17], the output y of the optimal *matched filter* (MF) receiver, when the phase of the received signal x_r is unknown, is

$$y = \frac{\left|X^H x_r\right|}{X^H X} \tag{6}$$

where X is the transmitted waveform. Similar to the previous discussions in Section II, the output of this detector when used with MCPC signals will exhibit relatively large sidelobe levels. These large sidelobes have the potential of causing false detections or even masking the presence of real targets. One method of overcoming the large sidelobe levels while maintaining a desired *probability of false alarm* (P_{FA}) is to use a *cell-averaging constant false alarm rate* (CA-CFAR) detector. The goal of CA-CFAR is to set a variable detection threshold level by estimating the interference power at the range resolution cell of interest (known henceforth as the *cell under test* (CUT)). It is clear that if the estimate of the interference power is larger than the actual power, the threshold will be set too high, which causes

a P_{FA} that less is than desired, leading to a reduction in detection performance. Conversely too low of an estimate results in an increase in P_{FA}.

While the intent of this paper is not to rigorously design optimal CFAR detectors, four varieties of CFAR schemes will be considered to further the conversation. In addition to the previously described CA-CFAR detector, the *least-of* CA-CFAR (LO-CA-CFAR) is considered, which works by comparing the power estimates in the leading and lagging reference cells and using the smaller of the two in the derivation of the threshold. The purpose of the LO-CA-CFAR is to prevent target masking, which occurs when the targets are present within the reference cells, causing the interference estimate to be too large. The LO-CA-CFAR attempts to circumvent this by only using the least-of the interference estimates. However, this methodology will fail when the targets are present within both the leading and lagging reference cells.

Another CA-CFAR scheme is called the *greatest-of* CA-CFAR (GO-CA-CFAR). The GO-CA-CFAR compares the interference estimates from the leading and lagging reference cells and chooses the greatest of the two. The purpose of this type of detector is to prevent false alarms caused by "spikes" in the interference power caused by clutter ridges or any other strong source of interference. However, this scheme will exacerbate target masking issues.

Yet another structure is called ordered-statistic CA-CFAR (OS-CA-CFAR). This structure works by ordering the power measurements in the reference cells from smallest to largest and taking assigning the Kth values as the estimate for the interference. Unlike the previously described CFAR methods, in OS-CA-CFAR the interference is estimated from only one sample instead of an average of samples. However, the threshold is still dependent on all of the samples as the Kth largest value in the ordered statistic is dependent on all of the samples. The purpose of this type of detector is to help prevent target masking.

After the interference at the CUT has been estimated, the next step is to assign an appropriate threshold to maintain a desired P_{FA}. This is accomplished through

$$T = \sqrt{\alpha \hat{I}} \tag{7}$$

where α is a *threshold multiplier*, and $\hat{I}$ is the interference estimate. The value of α in (7) is dependent on the number of training cells, the desired P_{FA}, and the CFAR type. For the basic CA-CFAR detector, α is calculated as [17]

$$\alpha_{\mathrm{CA}} = N\left(P_{\mathrm{FA}}^{-1/N} - 1\right) \tag{8}$$

where N is the number of training cells. Similar closed-form solutions for the threshold multiplier for the other CFAR detectors do not exist and must be solved for iteratively. For the LO-CA-CFAR detector, the equation to solve

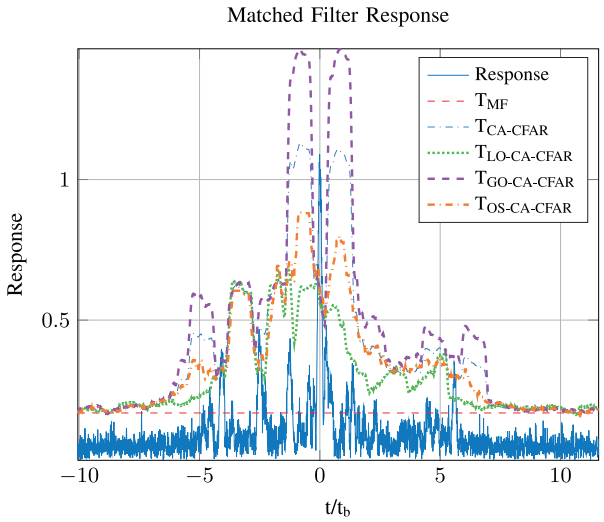

Fig. 2. MF response and various detection thresholds.

is [18]

$$\frac{P_{\mathrm{FA}}}{2} = \left(2 + \frac{\alpha_{LO}}{N/2}\right)^{-N/2} \times \left[\sum_{k=0}^{\frac{N}{2}-1} \binom{\frac{N}{2}-1+k}{k} \left(2 + \frac{\alpha_{LO}}{N/2}\right)^{-k}\right] \tag{9}$$

for the GO-CA-CFAR detector, the equation to solve is [18]

$$\frac{P_{\mathrm{FA}}}{2} = \left(1 + \frac{\alpha_{\mathrm{GO}}}{N/2}\right)^{-N/2} - \left(2 + \frac{\alpha_{\mathrm{GO}}}{N/2}\right)^{-N/2} \times \left[\sum_{k=0}^{\frac{N}{2}-1} \binom{\frac{N}{2}-1+k}{k} \left(2 + \frac{\alpha_{\mathrm{GO}}}{N/2}\right)^{-k}\right] \tag{10}$$

and for the OS-CA-CFAR detector, the equation to solve is [17]

$$P_{\mathrm{FA}} = \frac{N!\,(\alpha_{\mathrm{OS}} + N - k)!}{(N-k)!\,(\alpha_{\mathrm{OS}} + N)!} \tag{11}$$

where α_{OS} is an integer. Readers are referred to [17] for a more detailed analysis on CFAR techniques.

An example will now be given to further the discussion. Assume that a radar is employing 6×6 P3-based MCPC waveforms. Also, assume that there are seven targets located within the pulse response at $t/t_b = -4.0644$, $t/t_b = -2.4797$, $t/t_b = -1.2581$, $t/t_b = 0.0$, $t/t_b = 0.2806$, $t/t_b = 1.3834$, and $t/t_b = 5.5905$. Furthermore, assume that the signal to noise ratio at the receiver is 10 dB for the target at $t/t_b = 0$ and 0 dB for the remaining targets. Also, assume that a P_{FA} of 10^{-5} is desired. For all CFAR techniques, leading and lagging training samples each spanning $t/t_b = 1$, and leading and lagging guard samples each spanning $t/t_b = 0.333$ are used. As is typical [19], the value of K is set to three quarters of the total number of training samples for the OS-CA-CFAR detector.

Fig. 2 shows the MF response, the Neyman–Pearson detection threshold (labeled T_{MF}) as derived in [17] as well

TABLE II
Target Detection Results for the CFAR Detectors

t/t_b	CA	LO	GO	OS
−4.0644	✓	✓	✓	✓
−2.4797	✓	✓		✓
−1.2581				
0.0	✓	✓	✓	✓
0.2806				
1.3834				
5.5905	✓	✓		✓

as the various CFAR detection thresholds. The Neyman–Pearson threshold produces an excessive number of false alarms due to the large range sidelobe response, whereas the CFAR thresholds reduces the number of false alarms. Table II tabulates which targets are successfully detected with each CFAR detector. In this particular example, no detector was successful in detecting all seven targets. The remainder of this section will introduce the PSD algorithm as a means of improving the detection performance.

First, a new detection scheme, called the *beta detector* (BD), is introduced. The derivation of the BD relies on the fact that P3- and P4-based MCPC codes are unitary. That is, an $M \times M$ MCPC code multiplied by its conjugate transpose results in the $M \times M$ identity matrix $\boldsymbol{I}$. This property will be exploited to overcome the inherent problem of large MCPC ACF sidelobes.

As a radar receives a signal, it performs an estimation of the underlying bits by performing an FFT operation on the signal (readers are referred to [20] for more information on OFDM detection and technologies). It is important to note that this estimation process does not use a hard decoding scheme. In other words, the estimate of the underlying bits is simply the output of the FFT operation. Assuming a sampling period of t_s, a total of Mt_b/t_s estimates will be produced. These estimated bits are reconstructed into $M \times M$ MCPC matrices that are subsequently multiplied by the conjugate transpose of the transmitted MCPC sequence resulting in

$$\hat{\boldsymbol{\xi}}_{\boldsymbol{n}} = \hat{\boldsymbol{U}}_n \boldsymbol{U}^{*\mathsf{T}}, \quad n = 1, 2, \ldots, Mt_b/t_s. \tag{12}$$

Remembering that MCPC sequences are unitary, $\hat{\boldsymbol{\xi}}_{\boldsymbol{n}}$ in (12) will equal an $M \times M$ identity matrix when the estimated MCPC matrix $\hat{\boldsymbol{U}}_n$ equals the transmitted MCPC matrix $\boldsymbol{U}$. A vector of measurements $R(n)$ are taken on all n $\hat{\boldsymbol{\xi}}$ values such that

$$R(n) = \frac{\left|\text{tra}\left(\hat{\boldsymbol{\xi}}_{\boldsymbol{n}}\right)\right|^2}{M \cdot \text{sum}\left(\left|\hat{\boldsymbol{\xi}}_{\boldsymbol{n}}\right|^2\right) + \left|\text{tra}\left(\hat{\boldsymbol{\xi}}_{\boldsymbol{n}}\right)\right|^2} \quad n = 1, 2, \ldots, Mt_b/t_s \tag{13}$$

where tra$(\cdot)$ is the trace operation, and sum$(\cdot)$ is the sum of all elements in the matrix. When the estimated MCPC matrix equals the transmitted MCPC matrix, R in (13) will equal 0.5.

It is necessary to derive the statistical distribution of (13) to establish an appropriate detection threshold. The following derivations will be concerned with the null hypothesis where it is assumed that the only signal present is additive white Gaussian noise. For the null hypothesis, each element of $\hat{\boldsymbol{\xi}}_{\boldsymbol{n}}$ is normally distributed as $N(0, \sigma_e^2) + jN(0, \sigma_e^2)$, where the notation $N\left(0, \sigma^2\right)$ corresponds to a zero-mean normally distributed random variable with variance σ^2. Considering the numerator of (13), it is obvious that the trace operation of the elements of $\hat{\boldsymbol{\xi}}_{\boldsymbol{n}}$ will also be normally distributed as $N(0, M\sigma_e^2) + jN(0, M\sigma_e^2)$. The absolute square of the trace then becomes gamma distributed as $\Gamma\left(1, 2M\sigma_e^2\right)$.

Now considering the first term in the denominator of (13), the sum of the absolute squares of the elements of $\hat{\boldsymbol{\xi}}_{\boldsymbol{n}}$ is gamma distributed as $\Gamma\left(M^2, 2\sigma_e^2\right)$. Multiplying this gamma distribution by M results in the gamma distribution $\Gamma\left(M^2, 2M\sigma_e^2\right)$. The second term in the denominator of (13) is identical to the numerator. The resulting distribution takes the following form:

$$f = \frac{A}{A + B} \tag{14}$$

where $A = \Gamma\left(1, 2M\sigma_e^2\right)$ and $B = \Gamma\left(M^2, 2M\sigma_e^2\right)$. If A and B were independent, then (14) equates to $\beta\left(1, M^2\right)$, where β is the beta distribution. Strictly speaking, A and B are not independent; however, under the null hypothesis, remembering that A is the result of the summation of the M independent diagonal elements of $\hat{\boldsymbol{\xi}}_{\boldsymbol{n}}$ and B is the result of the summation of all M^2 independent elements of $\hat{\boldsymbol{\xi}}_{\boldsymbol{n}}$, as the value of M increases, A and B become more independent. If fact, it is easy to show that $M \geq 4$ results in (14) closely approximating the beta distribution. Now, assuming the desired *probability of false alarm* is equal to P_{FA}, the detection threshold T can be determined by solving

$$1 - P_{\text{FA}} = \frac{1}{\beta\left(1, M^2\right)} \int_0^{T_\beta} (1 - x)^{M^2 - 1}\, dx \tag{15}$$

for T_β.

The PSD algorithm begins by considering the MF response and BD response jointly. Now, returning to the example as defined in Table II, Fig. 3 depicts the beta response versus the MF response. The various shapes within the figure represent the individual target's effect on the overall joint response. Qualitatively, each target is easily discernible. The next step is to derive a new threshold parameter that will quantitatively detect the targets.

A polar representation of the data presented in Fig. 3 with an origin at (0, 0) is constructed and shown in Fig. 4. In this figure, as θ approaches 0, the ρ values are more heavily influenced by beta response and as θ approaches $\pi/2$, ρ is more heavily influenced by the MF response. The tangent of θ equals the ratio of the MF response to the beta response. A sample that has a maximum MF response (equal to 1) and a maximum beta response (equal to 0.5) will be located at $\theta \approx 1.1071$ with $\rho \approx 1.118$.

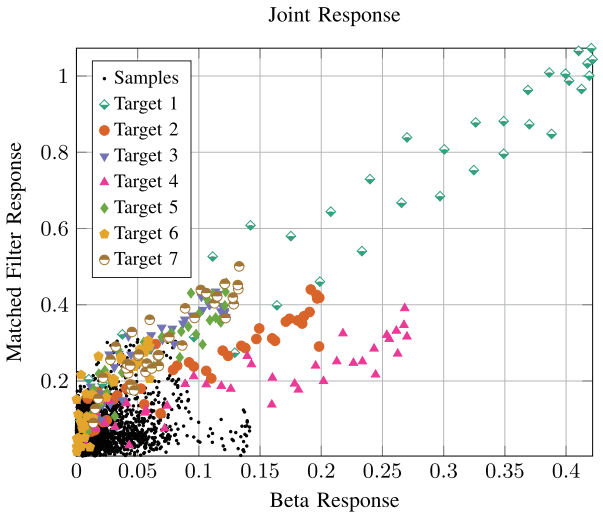

Fig. 3. Joint MF and beta response.

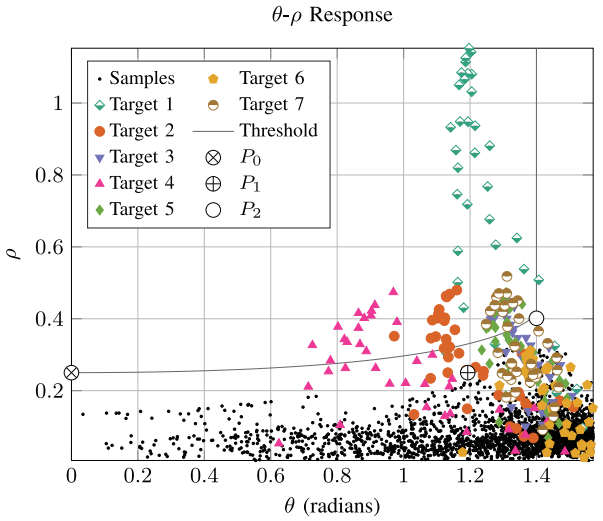

Fig. 4. Joint MF and beta response converted to polar coordinates. All samples within the borders of the threshold are declared detections.

Similar to the CA-CFAR approach, an interference estimate must be calculated from the available polar data. The approach taken is to use all samples less than $\theta_{I,\min}$ and greater than $\theta_{I,\max}$ for interference estimation. Through experimentation, based upon the observed polar responses of many trials, it has been found that $\theta_{I,\min} = 0.4$ and $\theta_{I,\max} = 1.4$ are acceptable values to use. Samples that are less than or equal to $\theta_{I,\min} = 0.4$ have beta responses that are greater than or equal to 2.3652 times larger than their MF responses, whereas samples greater than or equal to $\theta_{I,\max} = 1.4$ have MF responses that are greater than or equal to 14.1014 time larger than their corresponding beta responses.

Under the null hypothesis, the statistical distribution of samples below $\theta_{I,\min} = 0.4$ will closely resemble the same beta distribution as described in (14) where $p_\rho(\rho|H_0) = \beta\left(\rho; 1, M^2\right)$. As previously mentioned, the samples greater than $\theta_{I,\max} = 1.4$ are more heavily influenced by the MF response. Through examination of (6), under the null hypothesis, where only complex AWGN is present, the ρ samples will more closely follow a gamma distribution. This gamma distribution takes the following form:

$$p(\rho|a,b) = \text{Gamma}(\rho; a, b) = \frac{\rho^{a-1}}{\Gamma(a)\, b^a} \exp\left(\frac{-\rho}{b}\right). \tag{16}$$

The parameters a and b can be found using the maximum likelihood approach, as described in [21].

Because the ρ values at opposite sides of θ follow different statistics, two distinct threshold values for a given P_{FA} are found. For the beta distribution on the left-hand side of the polar response, this threshold is found by solving (15) for T_β. An exact solution for the threshold does not exist, but can be solved for numerically. Similarly, the threshold on the right-hand side is found through the inverse cumulative gamma distribution. That is, by solving

$$1 - P_{\text{FA}} = \frac{1}{b^a \Gamma(a)} \int_0^{T_\Gamma} x^{a-1} \mathrm{e}^{-x/b} dx \tag{17}$$

for T_Γ. Like the beta distribution, an exact solution for the threshold does not exist, but can also be solved numerically.

The question now is how to transition from the threshold as found through the beta distribution to the threshold as found through the gamma distribution. The approach taken here is to use quadratic Bèzier curves, which is defined as

$$B(t) = P_0(1-t)^2 + 2P_1 t(1-t) + P_2 t^2, \quad 0 \le t \le 1. \tag{18}$$

The path of a Bèzier curve begins at point $B(0) = P_0$, travels toward P_1 (without ever reaching P_1), and then turns and ends at $B(1) = P_2$.

The Bèzier points used to generate a threshold for the PSD algorithm are $P_0\left(0, T_\beta\right)$, $P_1\left(\theta_{\rho,\max}, T_\beta\right)$, and $P_2\left(\theta_{I,\max}, T_\Gamma\right)$. Through experimentation, a good choice for $\theta_{\rho,\max}$ is the θ location of the sample with the largest value of ρ. Furthermore, all samples greater than $\theta_{I,\max}$ are not considered for detection as any sample crossing the Bèzier detection threshold are almost assuredly the result of the large range sidelobes through the MF detector. There is no need to have a hard cutoff for samples at θ close to 0 as large sidelobes are not present in the output of the BD.

For the example case, the three Bèzier points are $P_0(0, 0.2501)$, $P_1(1.1931, 0.2501)$, $P_2(1.4, 0.4013)$ each of which are marked in Fig. 4. In examining Fig. 4, it is seen that the Bèzier threshold follows the same basic curve as the underlying interference samples.

Now, the PSD detection routine will be evaluated in term of its performance as compared to the previously described CFAR detectors. For the following example, the parameters used for the CFAR detectors are the same as those used in Fig. 2. For this test, a 6×6 P3-based MCPC sequence will be used to detect seven targets with a desired P_{FA} of 10^{-5}. One target is always placed at $t/t_b = 0.0$, whereas the others are randomly placed between $t/t_b = -6.0$ and $t/t_b = 6.0$ inclusive. The return from the target at $t/t_b = 0.0$ always has an SNR of 10.0 dB. The independent test

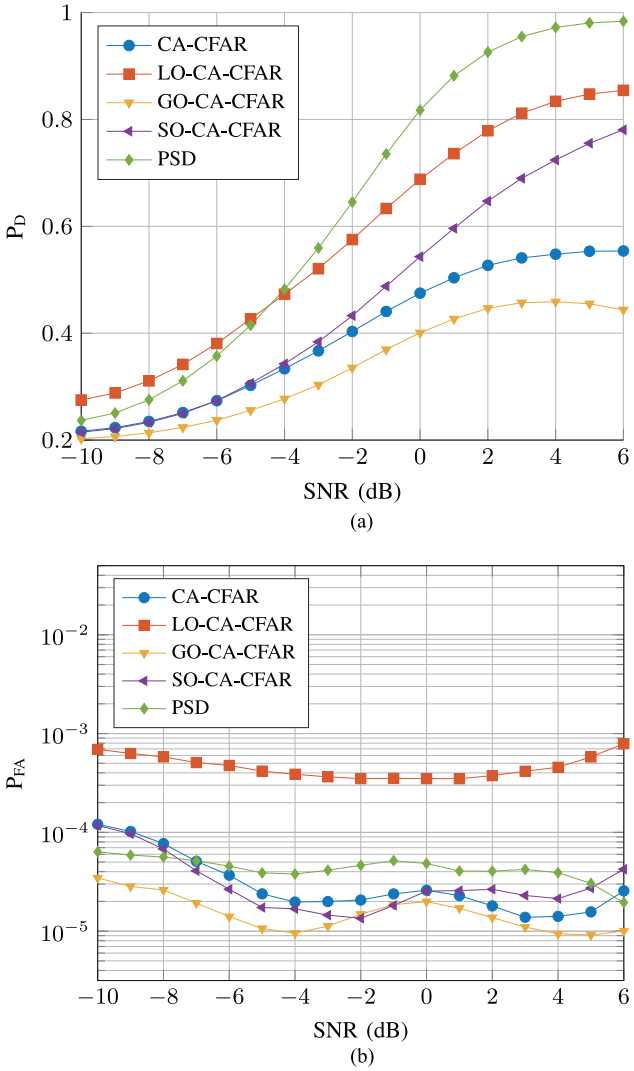

Fig. 5. Comparison of CFAR detection and PSD detection. (a) A P_D comparison between various CFAR thresholds and the PSD threshold, (b) A P_{FA} comparison between various CFAR thresholds and the PSD threshold

variable is the echo power from the targets not at $t/t_b = 0.0$. For each test, the return power from these targets will be equal and varied from -10.0 to 6.0 dB.

Fig. 5 shows the results of this test. Fig. 5(a) shows the probability of detections, where, in this case, it is equal to the total number of target detections divided by the total number of targets. It is clear from Fig. 5(b) that the detection performance of the PSD detector is superior to the CA-CFAR-based detectors.

Fig. 5(b) provides the P_{FA} in terms of the tested SNR. It is noted that none of the detectors achieves the desired P_{FA} of 10^{-5}. Nevertheless, the P_{FA} for the various detectors are relatively constant across all tested SNRs. It is observed that, out of all the CFAR detectors, the LO-CA-CFAR detector has the best detection performance. However, the LO-CA-CFAR detector also has the worst performance in terms of P_{FA}.

It is important to note that, as previously mentioned, the intent of this paper is not to rigorously design optimal CFAR detectors. It is therefore possible that the number of guard and training samples used in the various CFAR schemes could be altered to provide better performance. Fig. 5 should be considered in the context of showing that the PSD detector is comparable, and in some cases superior, to traditional CFAR detectors.

IV. DOPPLER MEASUREMENT

A major obstacle in achieving maximum system performance in multicarrier communication technologies such as OFDM is inter-carrier interference (ICI). ICI is caused by *carrier frequency offsets* (CFO) due, in part, to mismatches in the transmitter and receiver *local oscillators* (LO) as well as Doppler shifts within the communication channel. This ICI leads to the destruction of orthogonality within the communication link that inhibits the accurate transmission of data. However, unlike a traditional wireless communication scheme, the transmitter and receiver are collocated, which are assumed to share the same LO thus mitigating its effect on CFO. It can therefore be assumed that ICI is caused predominately due to Doppler shifts within the environment. The goal then is to measure the ICI in order to determine the equivalent Doppler shift caused by moving targets within the environment.

In an OFDM communication system, the received signal on subcarrier k in an AWGN channel with ICI has been well established as [22]

$$Y(k) = X(k)\,S(0) + \sum_{l=0, l\neq k}^{N-1} X(l)\,S(l-k) + n_k \qquad (19)$$
$$k = 0, 1, \ldots, N-1$$

where $X(k)$ is the transmitted modulated symbol on the kth subcarrier, and n_k is the additive Gaussian noise sample. $S(l-k)$ is the ICI coefficient between the lth and kth subcarrier, which is equated as

$$S(l-k) = \frac{\sin(\pi(\epsilon + l - k))}{N \sin\left(\frac{\pi}{N}(\epsilon + l - k)\right)} \cdot \exp\left(j\pi\left(1 - \frac{1}{N}\right)(\epsilon + l - k)\right) \qquad (20)$$

where ϵ is the normalized frequency offset given by $\epsilon = \Delta F/\Delta f$ (ΔF is the CFO, and Δf is the subcarrier spacing of the system).

In matrix notation (19) can be written as

$$\bar{Y} = \left(\bar{X}^{\intercal}\boldsymbol{S}\right)^{\intercal} + \bar{n} \qquad (21)$$

where $\bar{X} = [X(0), \ldots, X(N-1)]^{\intercal}$ is the transmitted modulated symbol vector through one bit interval (i.e., a single column of Section I) produced by (4), $\bar{Y} = [Y(0), \ldots, Y(N-1)]^{\intercal}$ is the corresponding received signal vector, $\bar{n} = [n_0, \ldots, n_{N-1}]^{\intercal}$ is the noise vector, and $\boldsymbol{S}$ is the ICI coefficient matrix. The pth-row and qth-column

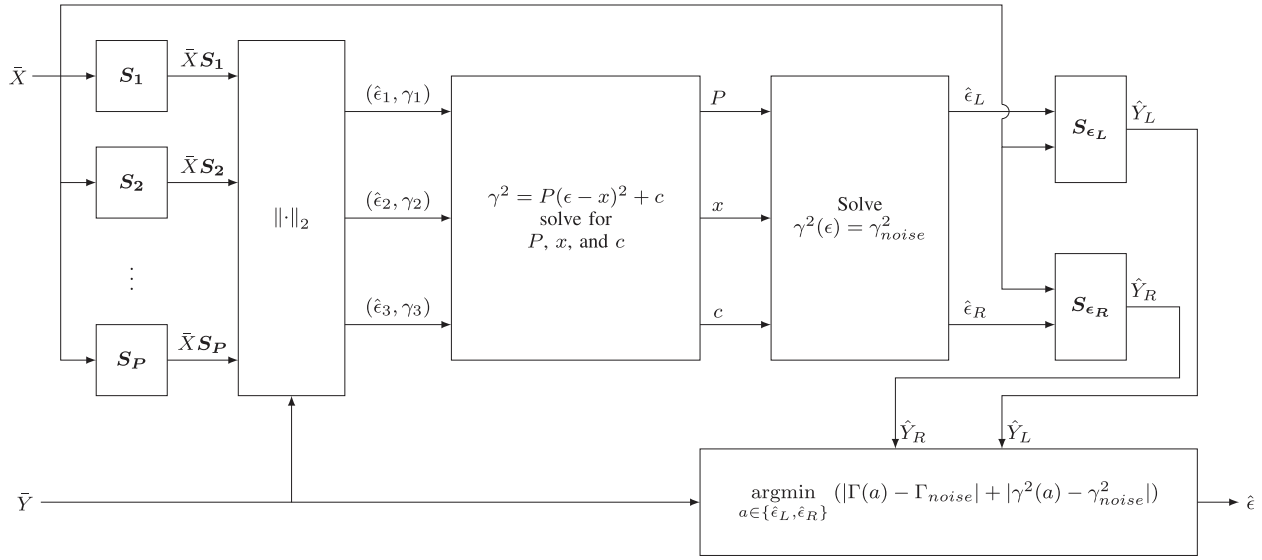

Fig. 6. Doppler measurement block diagram.

element of the $N \times N$ $\boldsymbol{S}$ matrix is

$$\boldsymbol{S}_{p,q} = \boldsymbol{S}_{p-q} = S(p-q) \tag{22}$$

resulting in the ICI coefficient matrix

$$\boldsymbol{S} = \begin{bmatrix} S_0 & S_{-1} & \cdots & S_{1-N} \\ S_1 & S_0 & \cdots & S_{2-N} \\ \vdots & \vdots & \ddots & \vdots \\ S_{N-1} & S_{N-2} & \cdots & S_0 \end{bmatrix}. \tag{23}$$

Assuming that the transmission bandwidth is sufficiently narrow, it can be shown that the Doppler shift from a target on a multicarrier signal is equivalent to the application of ICI. Suppose, for instance, that a multicarrier signal experiences a Doppler shift proportional to the subcarrier spacing. That is

$$\epsilon_{\text{Doppler}} = \frac{f_d}{\Delta f} \tag{24}$$

which is equivalent to the normalized frequency offset value ϵ as used in the calculation of the ICI matrix in (20).

The Doppler estimation technique proposed in this paper will be borrowed from [23], where a method was presented to perform blind ICI cancelation. However, unlike the channel equalization approach, this Doppler estimation technique is greatly simplified as the radar has perfect knowledge of the transmitted waveform. Although the normalized frequency offset due to the Doppler shift ϵ is unknown to the radar, we can quantize ϵ into P equally spaced values

$$\epsilon'_p = \epsilon_{\min} + (p-1) \cdot \Delta\epsilon,\ p = 1, 2, ..., P \tag{25}$$

where $\epsilon_{\min}$ is the smallest test value and $\Delta\epsilon$ is the uniform spacing between the normalized frequency offset estimates. $\Delta\epsilon$ can be calculated in terms of the maximum desired test value $\epsilon_{\max}$ by

$$\Delta\epsilon = \frac{\epsilon_{\max} - \epsilon_{\min}}{P}. \tag{26}$$

It is obvious that one of these P estimates will be the closest to the true normalized frequency offset ϵ.

Following along with the Doppler measurement receiver in Fig. 6, P parallel channels are built in the receiver where each branch uses one of the P quantized ϵ s to create the corresponding ICI coefficient matrix $\hat{\boldsymbol{S}}$. Hence, there are P ICI coefficient matrices $\hat{\boldsymbol{S}}_1$, $\hat{\boldsymbol{S}}_2$, ..., $\hat{\boldsymbol{S}}_P$ where the pth matrix corresponds to

$$\hat{\boldsymbol{S}}_p = \begin{bmatrix} S_p(0) & S_p(-1) & \cdots & S_p(1-N) \\ S_p(1) & S_p(0) & \cdots & S_p(2-N) \\ \vdots & \vdots & \ddots & \vdots \\ S_p(N-1) & S_p(N-2) & \cdots & S_p(0) \end{bmatrix} \tag{27}$$

and

$$S_p(l-k) = \frac{\sin\left(\pi\left(\hat{\epsilon}_p + l - k\right)\right)}{N \sin\left(\frac{\pi}{N}\left(\hat{\epsilon}_p + l - k\right)\right)} \cdot \exp\left(j\pi\left(1 - \frac{1}{N}\right)\left(\hat{\epsilon}_p + l - k\right)\right) \tag{28}$$

In every branch, using the ICI coefficient matrix estimates, an estimate of the received OFDM signal is calculated as

$$\hat{\boldsymbol{Y}}_p = \left(\boldsymbol{X}^{\mathsf{T}} \hat{\tilde{\boldsymbol{S}}}_p\right)^{\mathsf{T}} \tag{29}$$

where $\boldsymbol{X}$ is the $N \times M$ matrix of transmitted MCPC bits, and $\hat{\tilde{\boldsymbol{S}}}_p$ is an $N \times NM$ matrix where

$$\hat{\tilde{\boldsymbol{S}}}_p = \left[\, \hat{\boldsymbol{S}}_p\ \hat{\boldsymbol{S}}_p \cdots\ \hat{\boldsymbol{S}}_p \,\right]. \tag{30}$$

The one ϵ_p' that is the closest to the true value of ϵ will result in an estimate of the received signal matrix $\hat{\boldsymbol{Y}}_p$ that is closest to the received signal matrix $\boldsymbol{Y}$. Hence, the comparison of the distances between the P reproduced received signal matrices and the true received signal matrix are used to determine a coarse estimate of the frequency offset where the values of ϵ_p' that produce the smallest distances are determined to be the better estimates.

Let γ_p denote the distance between Pth estimated signal matrix and the received signal matrix such that

$$\gamma_p = \|\hat{\boldsymbol{Y}}_p - \boldsymbol{Y}\|_F \tag{31}$$

where $\|\cdot\|_F$ is the Frobenius norm. The value of the cost function γ with perfect normalized frequency offset estimation occurs when the ICI coefficient matrix estimate $\tilde{\boldsymbol{S}}$ exactly matches the true ICI coefficient matrix $\boldsymbol{S}$. The value of the cost function at this point is equal to

$$\gamma_{\text{noise}} = \|\boldsymbol{N}\|_F \tag{32}$$

where $\boldsymbol{N}$ is $N \times M$ the complex noise matrix whose elements $n_{i,j}$ are distributed as $n_{i,j} \sim [N\left(0, \sigma^2\right) + jN\left(0, \sigma^2\right)]$. Equation (32) can be equivalently written as

$$\gamma_{\text{noise}} = \sqrt{\sum_{i=1}^{N}\sum_{j=1}^{M}|n_{i,j}|^2}. \tag{33}$$

It can be shown that the absolute value of $n_{i,j}$ is Rayleigh distributed such that $|n_{i,j}| \sim R(\sigma)$. It can also be shown that the sum of the squares of $N \cdot M$ Rayleigh random variables is gamma distributed as

$$\sum_{i=0}^{NM-1}|\text{vec}(\boldsymbol{N})|^2 \sim \Gamma\left(NM, 2\sigma^2\right). \tag{34}$$

Thus, the expected value of γ_{noise} is

$$\begin{aligned} E[\gamma_{\text{noise}}] &= \sqrt{E[\Gamma\left(NM, 2\sigma^2\right)]} \\ &= \sqrt{2NM\sigma^2}. \end{aligned} \tag{35}$$

It is important to note that γ_{noise} is not necessarily the minimum value of the cost function, and, in fact, the probability that the minimum value of the cost function equals γ_{noise} is exactly equal to 0.

The square of the cost function (γ^2) can be approximated as a quadratic function as γ approaches its minimum such that

$$\gamma^2 = P(\epsilon - x)^2 + c \tag{36}$$

where x equals the ϵ value that minimizes γ^2 and c is the minimum value of γ^2. It is noted that (36) has three unknowns (P, x, and c), which can be fully solved for if three samples of the cost function γ^2 are available. Therefore, the smallest value of the cost function as well as its two smallest neighbors, labeled $(\hat{\epsilon}_1, \gamma_1)$, $(\hat{\epsilon}_2, \gamma_2)$, and $(\hat{\epsilon}_3, \gamma_3)$ at the output of the $\|\cdot\|_F$ block in Fig. 6, are now used to solve for these unknowns. The following system of equations can now be solved simultaneously

$$\begin{aligned} \gamma_1^2 &= P(\epsilon_1 - x)^2 + c \\ \gamma_2^2 &= P(\epsilon_2 - x)^2 + c \end{aligned}$$

and

$$\gamma_3^2 = P(\epsilon_3 - x)^2 + c$$

yielding

$$P = \frac{\gamma_1^2 - \gamma_2^2}{(\epsilon_1 - \epsilon_2)(\epsilon_2 - \epsilon_3)} - \frac{\gamma_1^2 - \gamma_3^2}{(\epsilon_1 - \epsilon_3)(\epsilon_2 - \epsilon_3)} \tag{37}$$

$$x = \frac{\epsilon_1^2\gamma_2^2 - \epsilon_2^2\gamma_1^2 - \epsilon_1^2\gamma_3^2 + \epsilon_3^1\gamma_1^2 + \epsilon_2^2\gamma_3^2 - \epsilon_3^2\gamma_2^2}{2(\epsilon_1\gamma_2^2 - \epsilon_2\gamma_1^2 - \epsilon_1\gamma_3^2 + \epsilon_3\gamma_1^2 + \epsilon_2\gamma_3^2 - \epsilon_3\gamma_2^2)} \tag{38}$$

and

$$c = \gamma_1^2 - P\left(\epsilon_1 - x\right)^2. \tag{39}$$

It is known that the square of the cost function γ^2 at the true value of the normalized frequency offset, ϵ_{true}, will equal

$$\gamma_{\text{noise}}^2 = 2NM\sigma^2 \tag{40}$$

which is the square of the value derived in (35). Solving $\gamma^2(\epsilon) = \gamma_{\text{noise}}^2$ yields two candidates for the estimate of the true normalized frequency offset

$$\begin{aligned} \hat{\epsilon}_L &= x + \frac{\sqrt{-4P\left(c - \gamma_{\text{noise}}^2\right)}}{2P} \\ \hat{\epsilon}_R &= x - \frac{\sqrt{-4P\left(c - \gamma_{\text{noise}}^2\right)}}{2P}. \end{aligned} \tag{41}$$

These two normalized frequency offset estimates are used to generate estimated ICI coefficient matrices ($\boldsymbol{S}_{\epsilon_L}$ and $\boldsymbol{S}_{\epsilon_R}$), which are subsequently used to generate two estimates of the received signal matrices ($\hat{\boldsymbol{Y}}_L$ and $\hat{\boldsymbol{Y}}_R$).

A second measurement must be used to determine whether ϵ_L or ϵ_R is the best estimate of ϵ. This measurement takes the following form:

$$\Gamma = \|\text{vec}(\hat{\boldsymbol{Y}}) - \text{vec}(\boldsymbol{Y})\|_1 \tag{42}$$

where $\|\cdot\|_1$ is the L^1-Norm operator and vec $(\cdot)$ is the vectorization operator. The vectorization operator simply converts the $N \times M$ matrix into a vector of length NM. The value of this cost function Γ with perfect ICI estimation equals

$$\Gamma_{\text{noise}} = \|\text{vec}(\boldsymbol{N})\|_1. \tag{43}$$

As previously shown, $|n_{i,j}|$ is Rayleigh distributed with a mean equal to $\sigma\sqrt{\frac{\pi}{2}}$. Therefore, the expected value of Γ_{noise} is expressed as

$$\text{E}\left[\Gamma_{\text{noise}}\right] = \text{E}\left[\sum_{i=0}^{NM-1}|\text{vec}(\boldsymbol{N})|\right] = NM\sigma\sqrt{\frac{\pi}{2}}. \tag{44}$$

Finally, an L^1 norm measurement is taken on the two reconstructed received signal matrix estimates and the actually

TABLE III
Radar Parameters for the Doppler Estimation Example

Parameter	Value
Carrier frequency	3 GHz
Wavelength (λ)	0.1 m
Channels	16
Modulation	4×4 P3 MCPC codes
Pulse width (τ)	100 μs
$f_{d,\max}$	10 kHz
Bandwidth	640 kHz
P	20
$\epsilon_{\min}$	-0.5
$\epsilon_{\max}$	0.5
$\Delta\epsilon$	0.05

received signal matrix, which are both compared to Γ_{noise}. The best estimate $\hat{\epsilon}$ is then determined as

$$\hat{\epsilon} = \underset{a\in\{\hat{\epsilon}_L,\hat{\epsilon}_R\}}{\operatorname{argmin}} \left(|\Gamma(a) - \mathrm{E}\left[\Gamma_{\text{noise}}\right]|\right) \tag{45}$$

where $\Gamma(a)$ is Γ evaluated at $\hat{\epsilon}_L$ and $\hat{\epsilon}_R$. With this estimated normalized frequency offset, the velocity estimate is calculated as

$$v = \frac{\hat{\epsilon}\Delta f C_0}{2f_c} \tag{46}$$

where C_0 is the speed of light.

A. Velocity Estimation Example

To help explain this velocity estimation routine, an example will be provided. Consider a radar operating at $f_c = 3$ GHz using $N = 16$ channels of 4×4 P3 MCPC-coded waveforms. If the maximum absolute relative velocity to the radar is expected to be $v_{\max} = 500$ m/s then the maximum absolute Doppler shift expected is equal to

$$f_{d,\max} = \frac{2f_c v_{\max}}{C_0}. \tag{47}$$

Also, suppose the desired maximum allowable absolute normalized frequency offset is $\epsilon_{\max} = 0.25$. This requirement can be satisfied by setting the operating bandwidth of the radar to

$$B = \frac{Nf_{d,\max}}{\epsilon_{\max}}. \tag{48}$$

This notional radar employs $P = 20$ ϵ_p estimates evenly distributed between -0.5 and 0.5 resulting in a $\Delta\epsilon$ spacing of 0.05. All radar parameters for this example are shown in Table III.

Upon signal detection, the twenty normalized frequency offset estimates are used to calculate twenty cost function values γ^2. As shown in Fig. 7, the smallest three consecutive γ^2 values along with their respective ϵ_p values are used to evaluate the quadratic fit of γ^2. Values for ϵ_L and ϵ_R (indicated by the left and right pointing triangles in the figure) are found by solving the quadratic fit for γ^2_{noise}. Γ values are obtained at ϵ_L and ϵ_R, which are then compared with Γ_{noise}. In this particular example, ϵ_L is chosen as the best estimate of ϵ because it minimizes the function defined in (45).

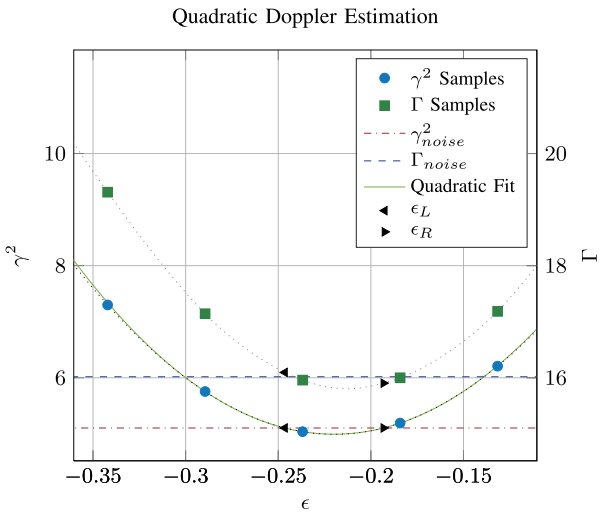

Fig. 7. Solid line is the quadratic fit of γ^2. ϵ_L and ϵ_R (indicated by the left and right pointing triangles) are found by solving the quadratic fit for γ^2_{noise}. Γ values are obtained at ϵ_L and ϵ_R, which are then compared with Γ_{noise}. ϵ_L is chosen as the best estimate of ϵ because it minimizes the function defined in (45).

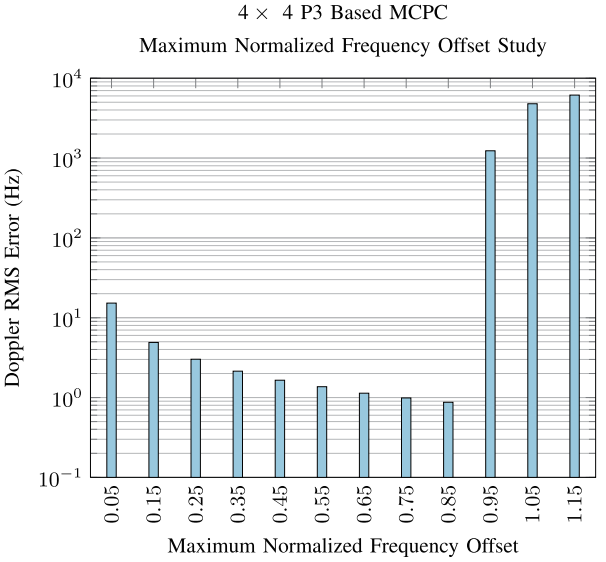

Fig. 8. Doppler RMS error at an SNR of 70 dB for various maximum normalized frequency offset values.

B. Velocity Estimation Design and Evaluation

As was hinted at in the previous example, there are design choices to be made. The design of the system must enforce a particular maximum expected absolute normalized frequency offset. A decision also must be made as to how many ϵ'_p samples need to be used. For the following discussion and figures, a carrier frequency of $f_c = 3.0$ GHz will be considered.

Fig. 8 shows the measured Doppler RMS error for different 4×4 P3-based MCPC sequences with a SNR of 70 dB using 15 ϵ'_p samples for different maximum absolute normalized frequency offset values. It is observed that the

best performance is achieved when the maximum normalized frequency offset is equal to approximately 0.85.

These results can be explained by first considering that enforcing a maximum normalized frequency offset is analogous to enforcing a specific subcarrier spacing. That is, decreasing the maximum normalized frequency offset is the same as increasing the subcarrier spacing, and, conversely, increasing the maximum normalized frequency offset is the same as decreasing the subcarrier spacing. It is also noted that the subcarrier spacing Δf is found in the numerator of the velocity calculation in (46). Thus, given a constant normalized frequency offset estimate error, a larger velocity estimation error is produced when the subcarrier spacing is larger (smaller maximum normalized frequency offset) and a smaller velocity estimation error is produced when the subcarrier spacing is smaller (larger maximum normalized frequency offset).

It is also noted that as the maximum normalized frequency offset gets greater than approximately 0.95, the Doppler estimation error increases rapidly. This is because the measurement of the normalized frequency offset becomes ambiguous as the frequency offset has shifted the received signal vector into adjacent subcarriers. For example, a normalized frequency offset of 1.1 will be incorrectly measured as an offset of 0.1.

The goal then is to design a system to maximize Doppler measurement performance. In light of the previous discussions, it is advantageous to enforce a maximum normalized frequency offset of approximately 0.85 by selecting a system bandwidth, given an expected maximum target radial velocity and number of subcarriers. Suppose the maximum expected radial velocity of a target is equal to $v_{\max}$. The total bandwidth of the system to achieve a maximum normalized frequency offset of 0.85 is found as

$$B_{\text{opt}} = \frac{2Nf_c v_{\max}}{0.85 \cdot C_0}. \tag{49}$$

Obviously, the design of this total bandwidth is limited by the physical capabilities of the notional radar system.

With this optimal bandwidth found, the next step is to determine the number of ϵ'_p necessary for adequate velocity estimation. Fig. 9 shows the RMS Doppler measurement error as a function of SNR for 4×4 P3-based MCPC sequences. The number ϵ'_p estimation samples tested are 5, 10, 15, and 20. For comparisons sake, the expected RMS Doppler measurement error of a traditional radar system with the same radar parameters (excluding the MCPC modulation) is also included. This expected error as given in [24] is

$$\sigma_v = \frac{\lambda}{2\tau\sqrt{2 \cdot S/N}} \quad \text{(m/s)}. \tag{50}$$

It is clear in Fig. 9 that the number of estimation samples sets a minimum bound for the best achievable Doppler RMS measurement error. For instance, examining Fig. 9, it is clear that by using $P = 10\ \epsilon'_p$ samples with a 4×4 P3-based MCPC sequence will result in a minimum Doppler RMS error of approximately 2.817 Hz.

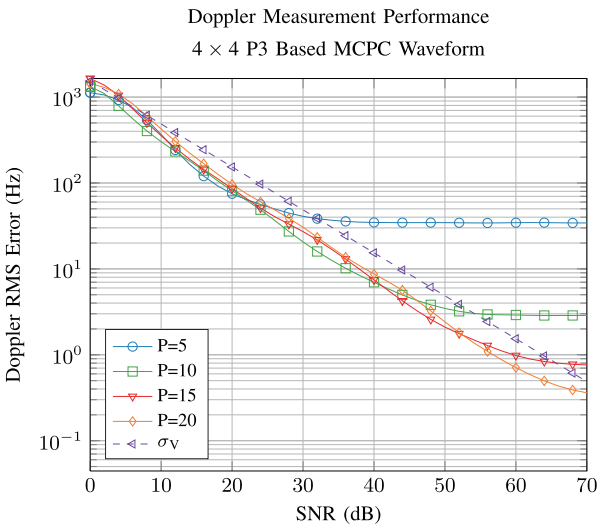

Fig. 9. Comparison of the RMS error resulting from the quadratic estimation of ϵ compared to the RMS error achieved in a traditional radar system as a function of SNR.

TABLE IV
Comparison of the Number of Valid Combinations and Corresponding Number of Bits per MCPC Sequence

Size	Combinations	Bits
3×3	4	2
4×4	16	4
5×5	64	6
6×6	512	9
7×7	4096	12
8×8	32 768	15
9×9	262 144	18
10×10	2 097 152	21

V. COMMUNICATIONS

This section will demonstrate the use of MCPC signals in a wireless communication context. For a system employing an $M \times M$ MCPC sequence, a total of $M!$ unique sequences can be generated (where ! is the factorial operator). Each of these unique sequences can be assigned a unique bit combination (i.e., a series of binary 1s and 0s). Suppose n such sequences have been identified. In order to ensure a complete code set (a complete code set contains all possible combinations of 1s and 0s) a maximum of

$$V = 2^{\lfloor \log_2(n) \rfloor} \tag{51}$$

can be used. Table IV provides the number of combinations of sequences and corresponding number of bits per sequence for various sizes of MCPC sequences.

A figure of merit in wireless communications is the *bit error rate* (BER), which is defined as the number of bit errors per unit time. As previously mentioned in Section IV, a major obstacle in achieving maximum system performance is ICI, which is caused by CFOs due, in part, to Doppler shifts within the communications channel. This ICI leads to

the destruction of orthogonality within the communication link that inhibits the accurate transmission of data.

Another property of a wireless communication channel that negatively impacts BER performance is multipath fading. Typically, fading channels in spread spectrum wireless systems such as OFDM demonstrate a Q-fold frequency diversity over the transmission bandwidth, where Q is, for example, 2, 3, or 4. Mathematically, this corresponds to

$$N\Delta f = Q\Delta f_c \tag{52}$$

where $N\Delta f$ is the bandwidth of the OFDM transmission, and Δf_c is the coherence bandwidth of the channel, which indicates that it is frequency selective over the entire transmission bandwidth but not over each subcarrier [25]. Specifically, with N carriers spaced across the entire bandwidth each carrier undergoes a flat fade with the correlation between the ith and jth subcarrier fades characterized by [25]

$$\rho_{i,j} = \frac{1}{1 + \left(\left(f_i - f_j\right)/\Delta f_c\right)^2} \tag{53}$$

where $\left(f_i - f_j\right)$ represents the frequency separation between the ith and jth subcarriers. The method used to generate these correlated fades is fully described in [26]. Now, the received signal vector in a fading channel with ICI is written as

$$\bar{Y} = \boldsymbol{B}\bar{X}\boldsymbol{S} + \bar{n} \tag{54}$$

where $\boldsymbol{B}$ is an $N \times N$ diagonal matrix equal to

$$\boldsymbol{B} = \begin{Bmatrix} \alpha_1 & 0 & \cdots & 0 \\ 0 & \alpha_2 & \ddots & \vdots \\ \vdots & \ddots & \ddots & 0 \\ 0 & \cdots & 0 & \alpha_N \end{Bmatrix} \tag{55}$$

where α_n is the correlated fading coefficient with Rayleigh statistics on channel n.

A. Channel Equalization and ICI Removal

The accuracy of the reception and interpretation of the transmitted data is dependent upon the mitigation of both the effects of the fading channel and the ICI. For clarity's sake, and without loss of generality, the following derivations will ignore the contributions from noise. The proposed fading channel equalization process begins by multiplying the received signal matrix by its conjugate transpose resulting

$$\begin{aligned} \boldsymbol{\zeta} &= \boldsymbol{Y}\boldsymbol{Y}^{*\mathsf{T}} \\ &= \boldsymbol{B}\boldsymbol{S}^{\mathsf{T}}\boldsymbol{X}^{\mathsf{T}}\boldsymbol{X}^{*\mathsf{T}}\boldsymbol{S}^{*}\boldsymbol{B}^{*\mathsf{T}}. \end{aligned} \tag{56}$$

Now, assuming there exists an estimate of the modulated transmitted symbol matrix (denoted $\hat{\boldsymbol{X}}$) and an estimate of the ICI matrix (denoted $\hat{\boldsymbol{S}}$), define

$$\begin{aligned} \boldsymbol{\rho} &= \left(\hat{\boldsymbol{X}}^{\mathsf{T}}\hat{\boldsymbol{S}}\right)^{\mathsf{T}}\boldsymbol{Y}^{*\mathsf{T}} \\ &= \hat{\boldsymbol{S}}^{\mathsf{T}}\hat{\boldsymbol{X}}\boldsymbol{X}^{*\mathsf{T}}\boldsymbol{B}^{*\mathsf{T}}\boldsymbol{S}^{*}. \end{aligned} \tag{57}$$

The channel equalization is completed by

$$\begin{aligned} \hat{\boldsymbol{Y}} &= \frac{\operatorname{diag}(\boldsymbol{\rho})}{\operatorname{diag}(\boldsymbol{\zeta})}\boldsymbol{Y} \\ &= \frac{\operatorname{diag}\left(\hat{\boldsymbol{S}}^{\mathsf{T}}\hat{\boldsymbol{X}}\boldsymbol{X}^{*\mathsf{T}}\boldsymbol{B}^{*\mathsf{T}}\boldsymbol{S}^{*}\right)}{\operatorname{diag}\left(\boldsymbol{B}\boldsymbol{S}^{\mathsf{T}}\boldsymbol{X}^{\mathsf{T}}\boldsymbol{X}^{*\mathsf{T}}\boldsymbol{S}^{*}\boldsymbol{B}^{*\mathsf{T}}\right)}\boldsymbol{B}\boldsymbol{S}^{\mathsf{T}}\boldsymbol{X} \end{aligned} \tag{58}$$

where $\operatorname{diag}(\cdot)$ is the diagonal operator and

$$\operatorname{diag}(\boldsymbol{A}) = \begin{bmatrix} A_{1,1} & 0 & \cdots & 0 \\ 0 & A_{2,2} & \ddots & \vdots \\ \vdots & \ddots & \ddots & \vdots \\ 0 & 0 & \cdots & A_{n,n} \end{bmatrix}. \tag{59}$$

If the estimates of the ICI matrix and the modulated transmitted signal matrix are perfect, it is easy to see that (58) reduces to $\hat{\boldsymbol{Y}} = (\boldsymbol{X}^{\mathsf{T}}\boldsymbol{S})^{\mathsf{T}}$, which is equal to the received signal with the effects of the fading channel removed. It is therefore concluded that the fading matrix $\boldsymbol{B}$ can be estimated as

$$\hat{\boldsymbol{B}} = \frac{\operatorname{diag}(\boldsymbol{\zeta})}{\operatorname{diag}(\boldsymbol{\rho})}. \tag{60}$$

The next step in the recovery of the transmitted symbols is to remove the effects of the ICI. With knowledge that the ICI coefficient matrix $\boldsymbol{S}$ is unitary, the ICI can be completely removed from the previously equalized signal, if we apply the following matrix multiplication:

$$\begin{aligned} \hat{\boldsymbol{X}} &= \left(\hat{\boldsymbol{Y}}^{\mathsf{T}}\boldsymbol{S}^{*\mathsf{T}}\right)^{\mathsf{T}} \\ &= \boldsymbol{X}. \end{aligned} \tag{61}$$

Through application of (61), the signal distortion caused by the fading channel and ICI can be effectively removed. However, before these techniques can be implemented, a method of obtaining estimates of the ICI and modulated transmitted symbol matrices must be established.

Similar to the Doppler estimation scheme proposed in Section IV, estimates of the normalized frequency offsets can be quantized into P equally spaced values between $\epsilon_{\min}$ and $\epsilon_{\max}$ where

$$\hat{\epsilon}_p = \epsilon_{\min} + \frac{1}{2}\Delta\epsilon + (p-1)\,\Delta\epsilon, \;\; p = 1, 2, \ldots, P \tag{62}$$

and $\Delta\epsilon$ is the spacing between the estimates defined by

$$\Delta\epsilon = \frac{\epsilon_{\max} - \epsilon_{\min}}{P - 1}. \tag{63}$$

P parallel channels are built in the receiver where each branch uses one of the P quantized ϵ s to create the corresponding ICI coefficient matrix $\hat{\boldsymbol{S}}$. Hence, there are P ICI coefficient matrices $\hat{\boldsymbol{S}}_1, \hat{\boldsymbol{S}}_2, \ldots, \hat{\boldsymbol{S}}_P$ where the pth matrix

corresponds to

$$\hat{\boldsymbol{S}}_p = \begin{bmatrix} S_p(0) & S_p(-1) & \cdots & S_p(1-N) \\ S_p(1) & S_p(0) & \cdots & S_p(2-N) \\ \vdots & \vdots & \ddots & \vdots \\ S_p(N-1) & S_p(N-2) & \cdots & S_p(0) \end{bmatrix} \tag{64}$$

and

$$S_p(l-k) = \frac{\sin\left(\pi\left(\hat{\epsilon}_p + l - k\right)\right)}{N\sin\left(\frac{\pi}{N}\left(\hat{\epsilon}_p + l - k\right)\right)} \cdot \exp\left(j\pi\left(1 - \frac{1}{N}\right)\left(\hat{\epsilon}_p + l - k\right)\right). \tag{65}$$

For every branch, using the quantized ICI coefficient matrix estimates, additional parallel branches are created, one for each valid MCPC combination. For each of these branches, a metric must be established to determine the best MCPC sequence estimate. We start by introducing

$$\xi = \left(\frac{\text{diag}\,(\boldsymbol{\rho})}{\text{diag}\,(\boldsymbol{\zeta})}\boldsymbol{Y}\right)^{*\mathsf{T}}\left(\hat{\boldsymbol{X}}^{\mathsf{T}}\hat{\boldsymbol{S}}_{\boldsymbol{p}}\right)^{\mathsf{T}}. \tag{66}$$

It is noted that (66) includes both the fading channel equalization as performed in (58) and the ICI cancelation as performed in (61). Assuming perfect estimations of the ICI matrix and the MCPC matrix, (66) reduces to

$$\begin{aligned} \xi &= \left((\boldsymbol{X}^{\mathsf{T}}\boldsymbol{S})^{\mathsf{T}}\right)^{*\mathsf{T}}(\boldsymbol{X}^{\mathsf{T}}\boldsymbol{S})^{\mathsf{T}} \\ &= \kappa\boldsymbol{I} \end{aligned} \tag{67}$$

where κ is a constant and $\boldsymbol{I}$ is an $M \times M$ identity matrix. Therefore, it is concluded that for a given normalized frequency offset estimate, the best estimate of the MCPC sequence will be the one that most resembles an identity matrix. A decision device is implemented where the best estimate of the MCPC sequence will be the one that maximizes

$$\beta = \frac{\left|\text{tra}\left(\hat{\boldsymbol{\xi}}\right)\right|^2}{M \cdot \text{sum}\left(\left|\hat{\boldsymbol{\xi}}\right|^2\right) + \left|\text{tra}\left(\hat{\boldsymbol{\xi}}\right)\right|^2}. \tag{68}$$

Now that the best MCPC sequence estimates have been found for each of the normalized frequency offset estimates, a decision has to be made on which of the $\hat{\epsilon}_p$ branches produces the most likely result. This is accomplished by first producing an estimate of the received signal that includes the effects of the estimated fading channel as well as the estimated ICI. The estimate of the fading channel was previously provided in (60) where $\boldsymbol{\zeta}$ is as given in (56) and $\boldsymbol{\rho}$ is as given in (57) with the ICI matrix estimation $\hat{\boldsymbol{S}}$ replaced by $\hat{\boldsymbol{S}}_p$ and the transmitted sequence estimation $\hat{\boldsymbol{X}}$ replaced by the best MCPC sequence estimate for the current ICI branch under investigation ($\hat{\boldsymbol{X}}_p$). The estimated received signal on branch p is then calculated as

$$\hat{\boldsymbol{Y}}_p = \hat{\boldsymbol{B}}\left(\hat{\boldsymbol{X}}_p^{\mathsf{T}}\hat{\boldsymbol{S}}_p\right)^{\mathsf{T}}. \tag{69}$$

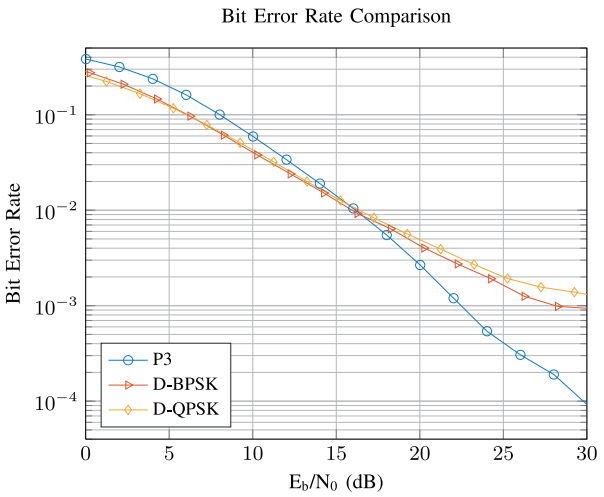

Fig. 10. BER performance in a fading channel with ICI.

A decision device is constructed where branch p, which minimizes

$$\Theta = \|\boldsymbol{Y} - \hat{\boldsymbol{Y}}\|_F \tag{70}$$

where $\|\cdot\|_F$ is the Frobenius norm, is deemed to be the best estimate of the transmitted MCPC sequence.

B. Simulation

This section will compare the effectiveness of MCPC-encoded signals and traditional phase-coded signals for digital communications in a fourfold frequency diverse correlated Rayleigh fading channel with ICI. The normalized frequency offset is randomly changed for each transmission with a uniform random number between -0.5 and 0.5 inclusive. The MCPC receiver uses three parallel branches with $\hat{\epsilon}_p$ the values of -0.25, 0, and 0.25 for ICI cancelation. In total, 4×4 P3 code sequences will be compared with differentially encoded *binary phase shift keying* (D-BPSK) and *quadrature phase shift keying* (D-QPSK) sequences. The *adjacent symbol repetition* (ASR) ICI self-cancelation scheme [27] will be applied to both the differentially encoded signals to mitigate the effects of ICI. ASR works by repeating the same symbol with opposite polarity on adjacent subcarriers, thus reducing the transmission rate by one-half. For all sequences, a 16-channel system will be employed, which results in the transmission of 4 MCPC codes per pulse.

Fig. 10 shows the results of this simulation. As compared to the performance of the ASR-coded signals (labeled D-BPSK and D-QPSK), the MCPC-encoded signal has similar performance at lower signal to noise ratios but performs dramatically better at higher power levels.

VI. CONCLUSION

This paper considered the optimization of radar performance within the structure imposed by a coded OFDM format required to achieve an acceptable communication link. In particular, the specific techniques, as introduced within

this paper, of using the MCPC sequences, as prescribed by Levanon and Mozeson, for simultaneous radar and wireless communication operations offer a significant improvement in the study, implementation, and performance of dual-use radar and communication waveforms and signal processing techniques.

In terms of radar detection performance, it was shown that the MF response of MCPC sequences produces sidelobe levels that are higher than those of other traditional pulse-compression radar waveforms. These high sidelobes produce false detections and mask the presence of real targets when using CA-CFAR detectors. A new detection scheme, termed PSD, was introduced as a means of overcoming these large autocorrelation sidelobes. Through simulation, it was shown that this new detector provides acceptable detection performance in multitarget environments. Also, a method of using MCPC waveforms to measure Doppler frequencies was introduced. It was shown that the RMS Doppler measurement error, when using the technique proposed in this paper, is superior to the performance of traditional radar systems.

In terms of communication performance, a novel method of exploiting the orthogonality of MCPC sequences to overcome the effects of multipath fading and intercarrier interference was introduced. Through simulation, it was demonstrated that the channel equalization approaches, as introduced within this paper, provide acceptable BER performance, as compared to traditionally modulated signals, in a fading channel with ICI.

REFERENCES

[1] N. Prasad, V. Shameem, U. Desai, and S. Merchant
Improvement in target detection performance of pulse coded Doppler radar based on multicarrier modulation with fast Fourier transform (FFT)
IEE Proc. Radar, Sonar Navig., vol. 151, no. 1, pp. 11–17, Feb. 2004.

[2] M. Mahmood and M. Bell
Non-linear processing for multicarrier MIMO radar for improved target resolution
In *Proc. Conf. Rec. 46th Asilomar Conf. Signals, Syst. Comput.*, Nov. 2012, pp. 1317–1322.

[3] G. Qin, B. Chen, and D. Chen
A new method for velocity estimation in multicarrier-frequency MIMO radar
In *Proc. IET Int. Radar Conf.*, Apr. 2009, pp. 1–4.

[4] S. Sen and A. Nehorai
Adaptive OFDM radar for target detection in multipath scenarios
IEEE Trans. Signal Process., vol. 59, no. 1, pp. 78–90, Jan. 2011.

[5] S. Sen, G. Tang, and A. Nehorai
Multiobjective optimization of OFDM radar waveform for target detection
IEEE Trans. Signal Process., vol. 59, no. 2, pp. 639–652, Feb. 2011.

[6] M. Wicks
Cognitive radar: A way forward
In *Proc. 2011 IEEE Radar Conf.*, May 2011, pp. 12–17.

[7] S. Sen and A. Nehorai
Target detection in clutter using adaptive OFDM radar
IEEE Signal Process. Lett., vol. 16, no. 7, pp. 592–595, Jul. 2009.

[8] C. Sturm and W. Wiesbeck
Waveform design and signal processing aspects for fusion of wireless communications and radar sensing
In *Proc. IEEE*, vol. 99, no. 7, pp. 1236–1259, Jul. 2011.

[9] P. van Genderen
A communication waveform for radar
In *Proc. 2010 8th Int. Conf. Commun.*, Jun. 2010, pp. 289–292.

[10] G. Lellouch and H. Nikookar
On the capability of a radar network to support communications
In *Proc. 2007 14th IEEE Symp. Commun. Veh. Technol. Benelux*, Nov. 2007, pp. 1–5.

[11] N. Levanon
Multifrequency complementary phase-coded radar signal
IEE Proc. Radar, Sonar Navig., vol. 147, no. 6, pp. 276–284, 2000.

[12] N. Levanon
Multifrequency radar signals
In *Proc. Record IEEE 2000 Int. Radar Conf.*, 2000, pp. 683–688.

[13] N. Levanon
Train of diverse multifrequency radar pulses
In *Proc. Proc. IEEE Radar Conf.*, 2001, pp. 93–98.

[14] N. Levanon and E. Mozeson
Multicarrier radar signal—Pulse train and CW
IEEE Trans. Aerosp. Electron. Syst., vol. 38, no. 2, pp. 707–720, Apr. 2002.

[15] E. Mozeson and N. Levanon
Multicarrier radar signals with low peak-to-mean envelope power ratio
IEE Proc. Radar, Sonar Navig., vol. 150, no. 2, pp. 71–77, 2003.

[16] B. Povovic
Complementary sets based on sequences with ideal periodic autocorrelation
Electron. Lett., vol. 26, no. 18, pp. 1428–1430, 1990.

[17] M. Richards
Fundamentals of Radar Signal Processing. New York, NY, USA: McGraw-Hill, 2005.

[18] M. Weiss
Analysis of some modified cell-averaging CFAR processors in multiple-target situations
IEEE Trans. Aerosp. Electron. Syst., vol. AES-18, no. 1, pp. 102–114, Jan. 1982.

[19] F. Nathanson, J. Reilly, and M. Cohen
Radar Design Principles: Signal Processing and the Environment. Scitech Publ., Raleigh, NC, 1999.

[20] A. Molisch
Wireless Communications (Ser. Wiley–IEEE). Hoboken, NJ, USA: Wiley, 2010.

[21] T. Minka
Estimating a gamma distribution
2002. [Online]. Available: http://research.microsoft.com/en-us/um/people/minka/papers/minka-gamma. pdf

[22] Y. Zhao and S.-G. Haggman
Sensitivity to Doppler shift and carrier frequency errors in OFDM systems-the consequences and solutions
In *Proc. IEEE 46th Veh. Technol. Conf. Mobile Technol. Hum. Race*, 1996, vol. 3, pp. 1564–1568.

[23] J. Ellinger, R. Depoy, J. Sanderson, K. Huang, and Z. Wu
Blind frequency offset estimation and intercarrier interference cancelation for FD-MC-CDMA systems in aerial vehicle communication
In *Proc. 2012 Mil. Commun. Conf.*, 2012, pp. 1–6.

[24] G. Curry
Radar System Performance Modeling (Ser. Artech House radar library), vol. 1. Norwood, MA, USA: Artech House, 2005.

[25] W. C. Jakes and D. C. Cox
Eds. *Microwave Mobile Communications*. Hoboken, NJ, USA: Wiley-IEEE Press, 1994.

[26] B. Natarajan, C. Nassar, and V. Chandrasekhar
Generation of correlated Rayleigh fading envelopes for spread spectrum applications
IEEE Commun. Lett., vol. 4, no. 1, pp. 9–11, Jan. 2000.

[27] Y. Zhao and S.-G. Haggman
Intercarrier interference self-cancellation scheme for OFDM mobile communication systems
IEEE Trans. Commun., vol. 49, no. 7, pp. 1185–1191, Jul. 2001.

John Ellinger (M'16) received the B.S. degree from The Ohio State University, Columbus, OH, USA, in 2003, the M.S. degree in from the University of Dayton, Dayton, OH, USA, in 2007, and the Ph.D. degree from Wright State University, Dayton, OH, USA, in 2016, all in electrical engineering.

He is currently with the United States Department of the Air Force, Wright-Patterson Air Force Base, Dayton, OH, USA.

Zhiping Zhang (M'16) received the B.S. degree in electrical engineering from Nankai University, Tianjin, China, in 2001, and the M.S. and Ph.D. degrees in intelligence science from Peking University, Beijing, China, in 2004 and 2011, respectively.

From 2011 to 2013, he was a Postdoctoral Research Fellow with the Department of Computer Science and Technology, Peking University. Since 2013, he has been a Research Faculty Member and Codirector with Broadband, Mobile and Wireless Networking Laboratory, Department of Electrical Engineering, Wright State University, Dayton, OH, USA.

Michael C. Wicks (S'81–M'89–SM'90–F'98) received the B.Sc. degree from Rensselaer Polytechnic Institute, Troy, NY, USA, in 1981, and the M.Sc. and Ph.D. degrees from Syracuse University, Syracuse, NY, USA, in 1985 and 1995, respectively, all in electrical engineering.

He was the U.S. Air Force Senior Scientist in sensors signal processing, specializing in the science and technology needed for superior air and space systems for intelligence, surveillance, reconnaissance, precision engagement, and electronic warfare. In 2011, he joined the University of Dayton, Dayton, OH, USA, where he is currently a Full Professor and Endowed Chair, Ohio Scholar for Sensor Exploitation and Fusion, and Distinguished Research Scientist.

Dr. Wicks was the recipient of the 2013 IEEE Picard Medal for Radar Technologies and Applications.

Zhiqiang Wu (M'02–SM'16) received the B.S. degree from Beijing University of Posts and Telecommunications, Beijing, China, in 1993, the M.S. degree from Peking University, Beijing, China, in 1996, and the Ph.D. degree from Colorado State University, Fort Collins, CO, USA, in 2002, all in electrical engineering.

From 2003 to 2005, he was an Assistant Professor with the Department of Electrical Engineering, West Virginia University Institute of Technology. In 2005, he joined the Department of Electrical Engineering, Wright State University, Dayton, OH, USA, where he is currently a Full Professor.